PHYSICAL REVIEW B **77**, 235307 (2008)

Transport anisotropy in $In_{0.75}Ga_{0.25}As$ two-dimensional electron gases induced by indium concentration modulation

Daniele Ercolani[*] and Giorgio Biasiol
Laboratorio TASC CNR-INFM, 34012 Trieste, Italy

Emiliano Cancellieri, Marcello Rosini, and Carlo Jacoboni
Dipartimento di Fisica, Università di Modena e Reggio Emilia and S3 CNR-INFM, 41100 Modena, Italy

Franco Carillo, Stefan Heun, and Lucia Sorba[†]
NEST CNR-INFM and Scuola Normale Superiore, 56126 Pisa, Italy

Frithjof Nolting
Paul Scherrer Institut, Swiss Light Source, 5232 Villigen-PSI, Switzerland
(Received 2 April 2008; published 12 June 2008)

A pronounced anisotropy is observed in the low-temperature mobility of a two-dimensional electron gas formed in an $In_{0.75}Ga_{0.25}As/In_{0.75}Al_{0.75}As$ quantum well grown on a GaAs substrate. We show that the mobility differences along [011] and $[01\bar{1}]$ directions are mainly due to In concentration modulations. Spatially resolved photoemission measurements show an asymmetric indium concentration modulation, correlated with the surface morphology observed by atomic force microscopy. A theoretical model considering conduction band energy modulations agrees well with the transport measurements. The identification of this mobility limiting mechanism allowed us to design and grow higher quality two-dimensional electron gases, needed for high indium content InGaAs device fabrication.

DOI: 10.1103/PhysRevB.77.235307 PACS number(s): 73.63.Hs, 73.50.Bk, 73.61.Ey, 79.60.Bm

I. INTRODUCTION

Two-dimensional electron gases (2DEGs) based on $In_xGa_{1-x}As/In_xAl_{1-x}As$ quantum wells (QWs) with high In concentration x offer potential advantages over $GaAs/Al_xGa_{1-x}As$ ones, both for studies in fundamental physics and for device applications, due to some peculiar properties such as low effective electron mass, large bare g factor, large Rashba coupling, and highly transmissive metal-semiconductor interfaces for $x \geq 0.75$. These features make $In_xGa_{1-x}As$ a promising candidate for the realization of spin-dependent mesoscopic devices.[1,2]

One of the main limitations for $In_xGa_{1-x}As/In_xAl_{1-x}As$ 2DEGs is the much smaller low-temperature electron mobility with respect to $GaAs/Al_xGa_{1-x}As$.[3–5] A high electron mobility is essential both for performance of mesoscopic devices and for studies of fundamental physics. It is, thus, of paramount importance to identify the mobility-limiting mechanisms in order to address them individually and improve the characteristics of this material system. Much work has already been devoted to this aim, through the comparison of experimentally measured electron mobilities with semiclassical scattering models.[6–11] The main scattering sources limiting the low-temperature mobility in this material system have been determined to be ionized impurity scattering and alloy disorder.[12–14] However, high-mobility $In_xGa_{1-x}As$ 2DEGs are often reported to show pronounced differences in mobility depending on the crystallographic direction of the current flow.[15–20] For QWs grown on the standard (100) surface, the mobility is highest along the $[01\bar{1}]$ direction and lowest along [011]. Such anisotropy is a clear indication of the presence of additional scattering mechanisms. Its origin is not fully understood, and it has been attributed to asymmetric strain relaxation,[15,16] interface roughness scattering,[17,18] or anisotropic spatial variations in residual strain.[19]

In this paper, we examine in detail the low-temperature transport properties of $In_{0.75}Ga_{0.25}As$ QWs, which manifest a strong mobility anisotropy that cannot be explained in terms of interface roughness scattering. A surface concentration map obtained with photoemission electron microscopy has allowed us to correlate, for the first time, the morphological properties of the sample surface to local variations in the indium concentration of the alloy. These local concentration modulations are shown to be responsible for significant spatial variations in the conduction band energy. Simulations show that these concentration modulations can explain a large part of the mobility differences. Our conclusions are confirmed by the increased mobility (in excess of $50\ m^2\ V^{-1}\ s^{-1}$) and reduced anisotropy of a QW sample containing a pure InAs layer.

II. EXPERIMENTAL DETAILS

The sample structures employed in this work include $In_{0.75}Ga_{0.25}As/In_{0.75}Al_{0.25}As$ QWs and are grown by solid source molecular beam epitaxy (MBE) on semi-insulating GaAs (100) substrates. The introduction of a compositionally graded buffer layer between the substrate and the lattice-mismatched $In_xGa_{1-x}As$ film allows total strain relaxation to take place.[21] Details on the buffer layer growth can be found elsewhere.[21,22] The active layer is composed of a 20-nm thick $In_{0.75}Ga_{0.25}As$ QW sandwiched between a lower 50-nm thick and an upper 120-nm thick $In_{0.75}Al_{0.25}As$ barrier. The

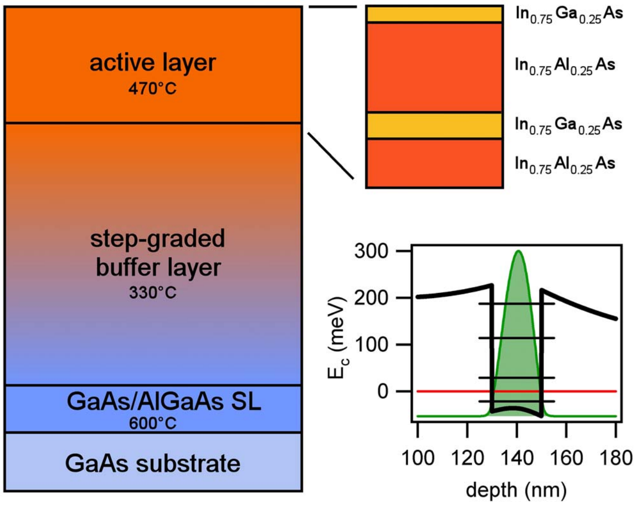

FIG. 1. (Color online) Growth sequence for sample HM1327, including active layer sequence. The growth temperature of each layer is indicated. The inset shows the conduction band minimum (black line) relative to the Fermi energy (red line) and carrier density profile (shaded area) for the QW, as calculated by a one-dimensional Poisson–Schrödinger solver for $n=3.0\times10^{15}$ m^{-2}. The lines running across the QW indicate the 2D subband energies.

structure of sample HM1327 is schematically depicted in Fig. 1. Indium concentrations are determined by high resolution x ray diffraction (XRD) measurements on calibration samples.

The samples are not intentionally doped, but a 2DEG is formed in the QW due to deep donor levels in the InAlAs barriers.[22] Given appropriate growth conditions, the carrier density in the quantum well is of the order of 3×10^{15} m^{-2}. The inset of Fig. 1 shows the conduction band minimum (CBM) and the carrier density profile in the growth direction for $n=3.0\times10^{15}$ m^{-2}. These have been calculated with the aid of a one-dimensional Poisson–Schrödinger solver,[23] using reference band gap parameters[24] and measured deep donor densities and Fermi level pinning at the surface.[22]

The sample surface shows a characteristic cross-hatch pattern of undulations aligned along the $\langle011\rangle$ crystallographic directions. An atomic force microscope (AFM) topograph of the sample surface is shown in the inset of Fig. 2. This surface morphology is typical for lattice mismatched growth[25] and, in the case of our samples, exhibits a root-mean-square (RMS) roughness of $\Delta\sim3$ nm and periodicities of $\Lambda\sim1.1$ μm and ~300 nm along the $[01\bar{1}]$ and $[011]$ directions, respectively. In these samples, the strain is released through the formation of a network of misfit dislocations, aligned along the two $\langle011\rangle$ directions, in the $In_xAl_{1-x}As$ step graded buffer. The last layer of dislocations is buried deep below the active layer at a depth of ~400 nm, and the active layer is, in average, unstrained.[21]

Hall bars (HBs) of different dimensions ($L\times w=260\times60$ and 40×10 μm^2; L is the length and w is the width of the HB, see inset of Fig. 2) have been fabricated (along both the $[011]$ and $[01\bar{1}]$ directions) either by optical lithography and wet chemical etching or—for the smaller ones—by electron beam lithography and reactive ion etching. Two different geometries and fabrication techniques have been employed to rule out fabrication related artifacts on the transport measurements. Electrical contact to the 2DEG is guaranteed by alloyed Ni/Ge/Au ohmic contacts (gray pads in the inset of Fig. 2). A surface aluminum gate covers the whole HB to allow the tuning of the carrier density. Due to the low Schottky barrier between Al and InGaAs exposed at the etched mesa borders, an insulating layer (~1 μm thick hard baked Shipley S1818 photoresist) is spinned on the sample prior to gate evaporation. This guarantees that no measurable leakage current flows between gate and 2DEG in a wide voltage range.

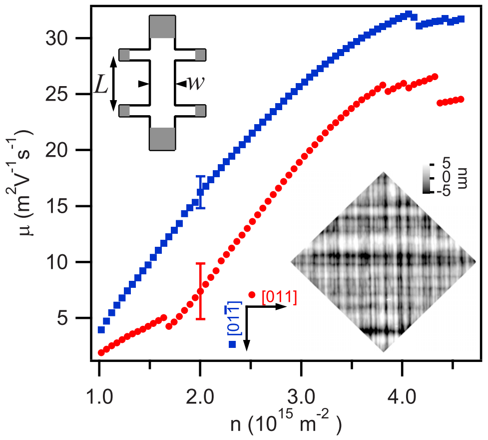

FIG. 2. (Color online) Electron mobility as a function of carrier density for sample HM1327, for Hall bars (HBs) oriented in two different directions. Squares refer to the $[01\bar{1}]$ oriented HBs (as in the schematic drawing), while circles refer to the $[011]$ oriented devices. The inset shows a 15×15 μm^2 AFM topography of the surface. The crystallographic directions are indicated below the graph.

Low-temperature magnetotransport measurements, with standard lock-in technique, have been performed on the HBs in a variable temperature, pumped ^{4}He refrigerator (with a base temperature of 1.5 K) or at 4.2 K in a liquid He bath. Carrier densities n are measured through the classical Hall effect (at $B=0.3$ T) and with frequency analysis of Shubnikov–de Haas oscillations. The latter also rule out the presence of parallel transport channels.

Photoemission electron microscopy (PEEM) is a powerful surface sensitive technique yielding compositional and chemical information with a high lateral resolution. We have used the PEEM microscope installed at the X11MA beamline of the Swiss Light Source in Villigen, Switzerland to obtain quantitative information on the spatial inhomogeneities of the $In_xGa_{1-x}As$ alloy composition. By using a parallel imaging system, the photoelectrons excited by soft x rays from the synchrotron are collected, selected in energy, and projected on a phosphor screen, from where the image is recorded with a charge coupled device (CCD) camera. This is repeated for several photoelectron kinetic energies. For each pixel, one can then plot the intensity as a function of energy, thus, obtaining local photoemission spectra. For our experiments, 120 eV photon energy has been chosen in order to have comparable intensities from the Ga 3*d* and In 4*d* core

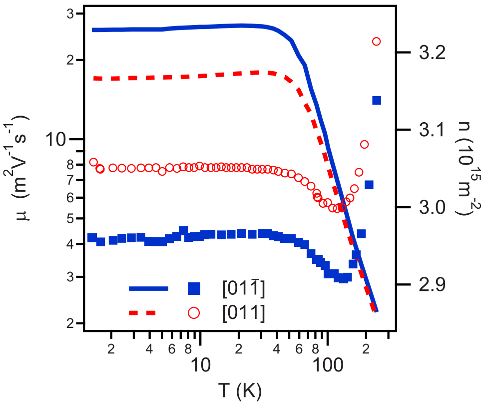

FIG. 3. (Color online) Temperature dependence of electron mobility (lines) and carrier density (symbols) for two devices aligned along the two crystallographic directions.

level emissions. To assess the local composition, we have acquired photoemission spectra in the kinetic energy range 93–103 eV, including both the In 4*d* and Ga 3*d* core level emissions, with an energy resolution of approximately 1 eV, sufficient to resolve the individual core levels. For a spatially resolved quantitative evaluation of the composition, we have fitted with an automated procedure all the spectra, from which a Shirley background was subtracted, with two doublets, corresponding to the two core levels. Due to the closeness in energy, one can safely assume the same photoelectron escape depth ($\sim$0.5 nm) for both core levels; the pixel-by-pixel In concentration is then given by the relative intensity (integrated in energy) of the In 4*d* level to the total one, (In 4*d*)/(In 4*d*+Ga 3*d*), normalized to the respective photoionization cross sections.[26] Additional details of the fitting procedure can be found elsewhere.[27,28]

III. TRANSPORT MEASUREMENTS

Transport measurements on sample HM1327 show a marked difference in electron mobility between HBs oriented along $[01\bar{1}]$ and $[011]$ directions. We have measured the mobility on several devices fabricated from different areas of the grown wafer. Although there is some variation from device to device, the mobility along the $[01\bar{1}]$ direction is systematically larger than the one along $[011]$. Figure 2 shows a comparison of the mobility along the two directions. The experimental points result from an average over four different devices of different sizes for each direction. The error bar is the maximum standard deviation of the average. The kinks in the curves (at $n \sim 1.7$ and around 4.0×10^{15} m^{-2}) are due to the fact that the range of carrier density attainable was different from device to device, thus, the calculated average shows an abrupt step when the number of curves averaged changes by one.

Figure 3 shows the temperature dependence of the electron mobility and the carrier density of two devices aligned along the two $\langle 011 \rangle$ directions. The carrier density shows only minor variations below 200 K, thus, it does not affect the mobility. The mobility difference is pronounced and independent of temperature at least up to $\sim$80 K, at which point it begins to decrease. This implies that even a thermal smearing of the order of $k_B T \sim 7$ meV is not sufficient to mask the anisotropy. At higher temperatures, phonons become the main scattering source for electrons, and the mobility in both directions decreases, while the difference tends to disappear since phonon scattering is isotropic.

The total mobility along each direction is limited by several different scattering mechanisms. According to Matthiessen's rule, valid for independent scattering mechanisms, the total mobility μ_T is given by

$$\frac{1}{\mu_T} = \frac{1}{\mu_A} + \frac{1}{\mu_B} + \ldots, \tag{1}$$

where μ_A, μ_B, …, are the mobilities determined by each scattering mechanism taken alone.[29]

Thus, the total mobility in each of the two orthogonal directions, μ_T^α (where the superscript α can be either $[01\bar{1}]$ or $[011]$) can be decomposed into an isotropic part μ_{iso}, equal for the two directions, and an anisotropic part μ_a^α, summed up as in Eq. (1). We define the mobility anisotropy between the two directions, $\Delta(1/\mu)$, as

$$\Delta(1/\mu) = \frac{1}{\mu_T^{[011]}} - \frac{1}{\mu_T^{[01\bar{1}]}} = \frac{1}{\mu_a^{[011]}} - \frac{1}{\mu_a^{[01\bar{1}]}}. \tag{2}$$

Note that $\Delta(1/\mu) \leq 1/\mu_a^{[011]}$, and in the case $\mu_a^{[01\bar{1}]} \gg \mu_a^{[011]}$, then $\Delta(1/\mu) \simeq 1/\mu_a^{[011]}$. $\Delta(1/\mu)$ is, thus, a lower limit for the reciprocal of the anisotropic part of the total mobility, in particular for the direction in which the anisotropic scattering mechanism is stronger.

We can compare $\Delta(1/\mu)$ with semiclassical models of scattering in 2DEGs taking into account the possible anisotropies. In particular, the scattering mechanisms usually taken into account in InGaAs alloys are ionized impurity scattering (both due to local and remote impurities), alloy disorder scattering (due to local potential fluctuations in the crystal at the atomic scale), and interface roughness scattering (due to the nonperfect planarity of interfaces).[9] These scattering mechanisms have been successfully modeled with a semiclassical approach in the 1980s.[6,9] Among the three mechanisms, the only one capable of introducing an anisotropy is the interface roughness scattering. We have verified that the surface topography of samples grown only up to the lower or upper QW interface is virtually identical with that of the whole structure, allowing us to use the surface topography as a model of the interfaces of the QW. The surface cross-hatch roughness (and, thus, interface roughness) exhibits strong differences in the two $\langle 011 \rangle$ directions. The mobility limit, due to interface roughness scattering μ_{IR}, in the case of an InGaAs QW, can be numerically calculated (following the work of Gold[9]) as a function of Δ and Λ, the height and length parameters of the interface roughness, respectively. We obtain these parameters from the AFM surface topographs of the sample, as the one shown in the inset of Fig. 2. The height parameter of the roughness has been taken to be its RMS roughness, $\Delta = 3$ nm, while the length

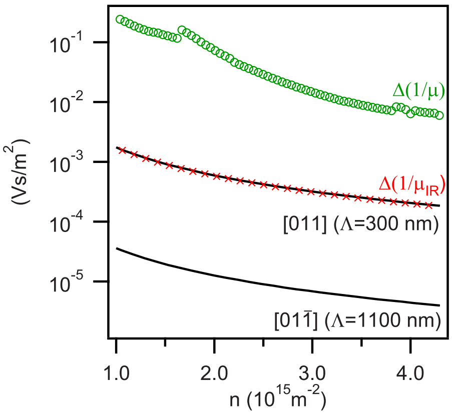

FIG. 4. (Color online) Measured mobility anisotropy $\Delta(1/\mu)$ [defined in Eq. (2)] between the two $\langle 011\rangle$ directions (circles) compared to the calculated reciprocal mobility according to the semiclassical model of Gold,[9] considering the interface roughness scattering for a QW with height parameter $\Delta=3$ nm and length parameter $\Lambda=300$ (1100) nm for the [011] ([01$\bar{1}$]) direction (lines). The crosses are the calculated values for $\Delta(1/\mu_{IR})$.

parameter was associated to the average period of the undulations in each direction: $\Lambda=300$ nm for [011] and $\Lambda=1100$ nm for [01$\bar{1}$].

The results of these calculations are plotted as $1/\mu_{IR}$ in Fig. 4. It is clear that, as the characteristic length increases, this scattering mechanism becomes less and less effective, and $\mu_{IR}^{[01\bar{1}]} \gg \mu_{IR}^{[011]}$. However, $\Delta(1/\mu_{IR})=1/\mu_{IR}^{[011]}-1/\mu_{IR}^{[01\bar{1}]}$ ($\sim 1/\mu_{IR}^{[011]}$ due to the large anisotropy), is two orders of magnitude smaller than the experimental values of $\Delta(1/\mu)$. This shows that interface roughness scattering provides a negligible contribution to the large observed anisotropy.

IV. INDIUM SURFACE CONCENTRATION MAPS

We have performed PEEM measurements to asses possible inhomogeneities of In concentration in the $In_{0.75}Ga_{0.25}As$ QW layer. Photoelectron spectroscopy is an extremely surface-sensitive technique, and, thus, a dedicated sample has been grown by MBE for this experiment. Its structure is nominally identical to that of HM1327 (Fig. 1), but the growth was stopped at the upper interface of the $In_{0.75}Ga_{0.25}As$ QW in order to access directly the QW composition. The sample was then rapidly cooled to 70 °C and exposed to an As_4 flux of about 2×10^{-5} Torr for 2 h to cap the surface with a protective As layer.[30] After exposure to air and transfer from the growth to the experimental chamber, the protective As layer was thermally removed *in situ* in ultrahigh vacuum by heating the sample to 410 °C until a clear (2×4) reconstruction was observed by low-energy electron diffraction. This provides an as-grown surface, free of contaminants that would impede the composition measurements. The morphology of the surface after the decapping process and the PEEM measurements was checked *ex situ* by AFM [see Fig. 5(a)] and scanning electron microscopy (SEM), and is consistent with that of the samples used for transport measurements.

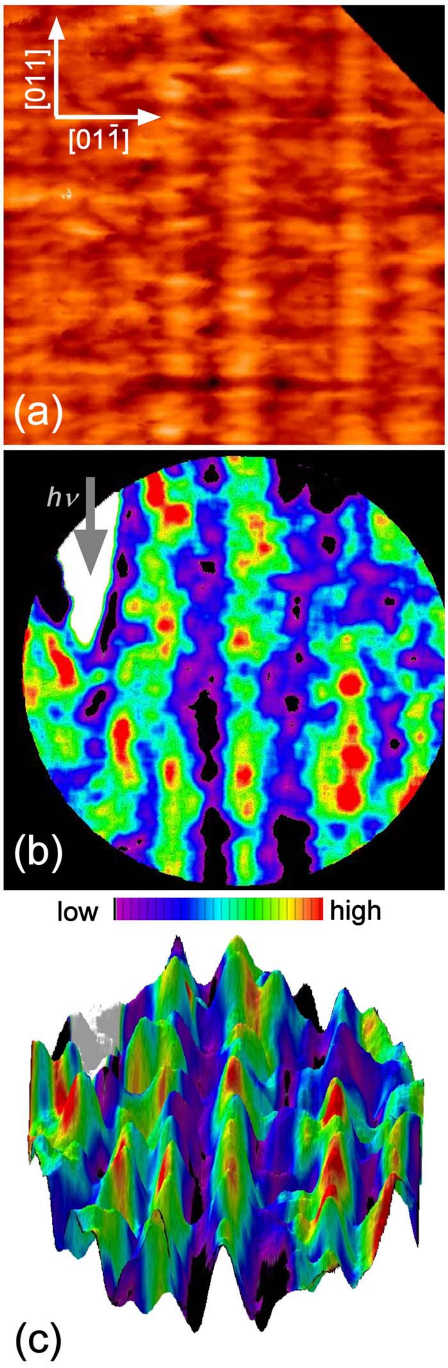

FIG. 5. (Color online) (a) 10×10 μm^2 AFM surface topography and (b) surface indium concentration map from the same area of the sample. The white area in (b) is the shadow of the x ray beam cast by a nearby 2 μm high defect. The arrow indicates the in-plane direction of the photon beam for the PEEM measurement. (c) A three-dimensional representation of the AFM topography of (a), colored with the indium concentration map of (b).

A 10×10 μm^2 In concentration map is shown in Fig. 5(b). Indium concentration modulations are observed on the sample, which are clearly aligned along the [011] direction. The In concentration values in the imaged area range from 96.2% to 96.9%, while the full scale of the colormap used for the image in Fig. 5(b) is from low=96.4% to high

$=96.8\%$. The RMS variation in the In concentration is 0.1%, with a clear asymmetry between the horizontal ($\mathrm{RMS}_{[01\bar{1}]}=0.09\%$) and the vertical direction ($\mathrm{RMS}_{[011]}=0.06\%$).

These concentration values are larger than the bulk composition measured by XRD ($x\sim 0.75$), likely due to indium surface segregation effects.[31] In fact, the apparent compositions observed with our technique are an average across the few topmost atomic layers, weighted with a photoelectron intensity exponentially decaying into the sample with an escape depth of about 0.5 nm,[32] and, thus, the surface segregation increases the measured In concentration. Our measured values are consistent with the presence of three monolayers of pure InAs above the $In_{0.75}Ga_{0.25}As$ layers. The composition fluctuations in the bulk, partly masked by the InAs segregated layers, then turn out to be 72.8%–77.9% full scale, with a $\mathrm{RMS}_{[01\bar{1}]}$ ($\mathrm{RMS}_{[011]}$) variation of 0.7% (0.5%) in the In concentration.

The presence of a defect close to the PEEM field of view has allowed us to directly compare the AFM surface topography with the photoemission spectra in the same area. The defect has been directly imaged with low energy electron microscopy (LEEM) during the PEEM session and, being ~ 2 μm high, casts a visible shadow in the PEEM field of view [white in Fig. 5(b)]. The comparison of LEEM and *ex situ* SEM images has allowed us to unambiguously identify the defect and take AFM topographs of the same area. The AFM topograph of the defect has enabled us to reconstruct the shadow position, allowing us to align the AFM topograph [Fig. 5(a)] to the PEEM images [Fig. 5(b)], as shown in Fig. 5(c).

When compared to the AFM topography, the indium concentration fluctuations are clearly related to surface morphology, with higher concentration on the top of the ridges and lower concentration on the bottom of the valleys aligned along the [011] direction. In the orthogonal direction, such correspondence seems to be much weaker. This does not exclude, however, an In accumulation on the top of the ridges also in this direction. In fact, several factors could mask the concentration modulation in the PEEM measurement. First, the dimension of the ridges parallel to the $[01\bar{1}]$ direction is only slightly larger than the spatial resolution (~ 100 nm) of the PEEM; second, small drifts (of the order of 100 nm) in the sample position during the energy scan (which takes several hours) are difficult to detect and to compensate for, given the absence of sharp and well localized features. Such small drifts, while not substantially affecting the measurement on the μm-sized ridges along the [011] direction, can lead to a loss of information on the ~ 300 nm ridges along $[01\bar{1}]$.

The PEEM-measured compositional fluctuations can be translated into conduction band energy modulations by first considering the total band gap variations due to indium concentration and then the fraction of these modulations affecting the CBM. This has been done using the suggested parameters given by Ref. 24 for InAs and GaAs, interpolating them linearly or using the suggested bowing parameters to obtain the energy of the $In_xGa_{1-x}As$ conduction band minimum as a function of indium concentration, x. We define $\Delta E_c(x)=E_c(x)-E_c(0.75)$ to be the energy variation of the CBM with respect to the CBM of the XRD-determined average concentration as a function of the local indium concentration x.

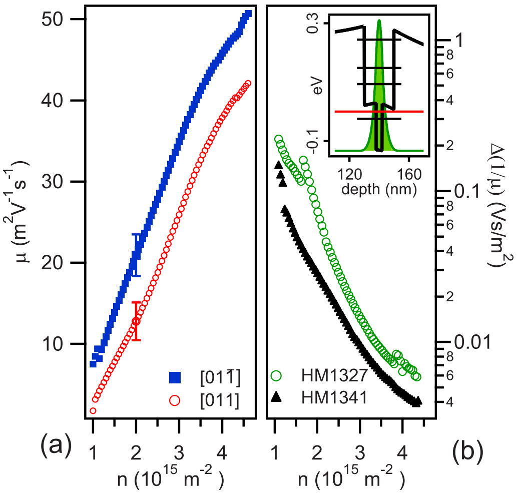

FIG. 6. (Color online) (a) Electron mobility as a function of carrier density for sample HM1341 along both ⟨011⟩ directions. (b) Mobility anisotropy $\Delta(1/\mu)$ for both sample HM1327 (InGaAs QW) and HM1341 (InAs inserted QW). Inset: CBM and carrier density profile for HM1341.

The above peak-to-peak In concentration variation implies a 44 meV peak-to-peak ΔE_c. If we compare this value with the Fermi energy of the electrons with respect to the two-dimensional (2D) subband bottom (21 and 10 meV at $n=3.0$ and 1.5×10^{15} m^{-2}, respectively), we understand that these fluctuations must have a strong influence on the electronic transport.

V. InAs QUANTUM WELL

To confirm the strong influence that compositional fluctuations have on electron transport, we have measured the low-temperature Hall mobility of a sample, HM1341, which is nominally identical to the previous one except that at the center of the 20-nm thick $In_{0.75}Ga_{0.25}As$ QW, a layer of strained InAs has been inserted. A thickness of 4 nm has been chosen for the InAs layer since it lies well below the critical thickness of InAs on $In_{0.75}Ga_{0.25}As$ but still ensures a sensible increase in electron mobility.[14] The insertion of an InAs layer is expected to reduce the mobility anisotropy since in a binary alloy no compositional fluctuation can take place.

Figure 6(a) shows the mobility as a function of the carrier density for devices aligned along the two crystallographic directions. As for Fig. 2, the experimental points in Fig. 6(a) are the results of an average over several devices, and the error bars represent the standard deviation of the average. The mobility along the $[01\bar{1}]$ direction exceeds 50 m^2 V^{-1} s^{-1} at a charge density of 4.5×10^{15} m^{-2}.

Similar to what has been observed for sample HM1327 (Fig. 2), the mobility along [011] is systematically lower than along $[01\bar{1}]$. However, as shown in Fig. 6(b), the mobility anisotropy for the InAs-inserted sample (HM1341) is systematically smaller than for the InGaAs QW (HM1327). This indicates that the asymmetric scattering mechanism is strongly reduced by the insertion of an InAs layer.

In fact, such insertion in the QW reduces the In concentration variation and, thus, the amplitude of the CBM modulations, increasing the overall mobility and reducing its asymmetry. The remaining mobility asymmetry is likely maintained by several concurrent causes: first, only approximately 50% of the wave function is contained in the InAs layer (see inset of Fig. 6) so the electrons are still sensitive to the CBM fluctuation in the InGaAs part of the QW. Second, although in the InAs layer, the composition cannot fluctuate, there may be a modulated strain field present due to the surrounding InGaAs, which alone is capable to alter the CBM energy. Last, the InAs/InGaAs interfaces exhibit the same roughness as discussed in Sec. III, but this time on a narrower well, where they are likely to have a much stronger effect (the mobility limit given by the interface roughness scattering is proportional to the sixth power of the QW width[9]).

VI. THEORETICAL MODEL

In order to evaluate the contribution of the fluctuations of the bottom of the conduction band to the electron mobility, we have calculated the conductance along the two crystallographic directions. Since this is the only nonisotropic contribution to electron conductance, similar to the mobility [cf. Eq. (2)], we can define a conductance anisotropy as

$$\Delta(1/G) = \frac{1}{G_T^{[011]}} - \frac{1}{G_T^{[01\bar{1}]}} = \frac{1}{G_a^{[011]}} - \frac{1}{G_a^{[01\bar{1}]}}, \tag{3}$$

where G_T and G_a are the total conductance and the anisotropic contribution,[33] respectively. To this aim, the Landauer approach has been used.[34,35] Within this approach, the conductance along one direction of a 2D sample is given by

$$G(E) = \frac{2e^2}{h}\sum_n T_n(E), \tag{4}$$

where the sum is extended over all the channels having transverse energy lower than the total energy E.

To implement the Landauer approach, we have modeled the experimental devices as square regions with two open boundaries. The inner region is described by means of a 2D potential $V(x,y)$, and the open boundaries are placed at $x=0$ and $x=x_{\max}$ or at $y=0$ and $y=y_{\max}$, depending whether the conductance is evaluated along the $[01\bar{1}]$ or the $[011]$ crystallographic direction, respectively.

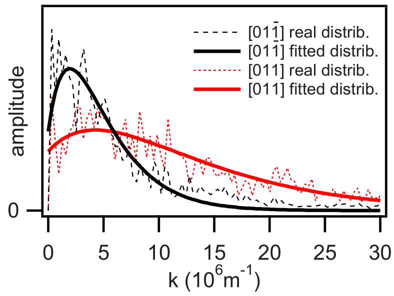

FIG. 7. (Color online) Fourier transforms of the surface roughness profiles for the $[01\bar{1}]$ and $[011]$ directions (black and red, respectively). The dashed lines are the Fourier transform of real data, while the solid lines are the fits $\Theta_{[01\bar{1}]}$ and $\Theta_{[011]}$ [see Eqs. (7) and (8)] with: $A_0=8.37\times10^{-19}$, $A_1=7.14\times10^5$, $A_2=3.76\times10^{-7}$, $A_3=1.54\times10^{-19}$, $A_4=2.89\times10^6$, and $A_5=1.4\times10^{-7}$.

The numerical evaluation of Eq. (4) needs, for every simulated device and for every crystallographic direction, the transmission coefficients of all the open channels at a given energy. In the case of 4 μm wide devices, at an energy value of $E=30$ meV, this corresponds to the evaluation of about $N(E)=200$ transmission coefficients. Since the numerical evaluation of each transmission coefficient is very resource consuming, we approximate Eq. (4) by means of

$$G(E) = \frac{2e^2}{h}N(E)\tilde{T}(E), \tag{5}$$

where $\tilde{T}(E)$ is the transmission coefficient of an incident wave function given by a linear superposition of the open channels as

$$\Psi(x,y) = \frac{1}{\sqrt{N}}\sum_{n=1}^{N}\phi_n(x)\frac{1}{\sqrt{2\pi}}e^{ik_ny}. \tag{6}$$

Here $\phi_n(x)$ is the transverse wave function of the n-th open channel, $k_n=\sqrt{2m^*(E-E_n)}/\hbar$ is the longitudinal wave vector, $E-E_n$ the relative kinetic energy, and m^* the effective mass. Equation (5) reproduces Eq. (4) in the case of large devices. In this case, the interference between the different components of Ψ gives a large number of terms whose contribution is expected to average to zero.

In order to simulate systems as close as possible to the real situation, line scans of actual AFM measurements along the two crystallographic directions have been considered. Then, the amplitude distributions of the Fourier components of several profiles of real devices have been fitted by means of the functions

$$\Theta_{[01\bar{1}]} = A_0(k+A_1)e^{-A_2k} \tag{7}$$

and

$$\Theta_{[011]} = A_3(k+A_4)e^{-A_5k}. \tag{8}$$

In Fig. 7, the Fourier transforms of the profiles in the two directions are shown, together with the best fit using Eqs. (7) and (8).

By using the two above fitting functions, we can generate at will random surfaces with the morphological characteristics of the real ones. To this purpose, we just need to introduce a random phase to each Fourier component when the Fourier antitransforms of Eqs. (7) and (8) are performed. In this way, random profiles $f_{[011]}(x)$ and $f_{[01\bar{1}]}(y)$ are generated having the same characteristics of the real ones. Then, the surface $S(x,y)$ of the 2D simulated device is calculated as the sum of $f_{[011]}(x)$ and $f_{[01\bar{1}]}(y)$:

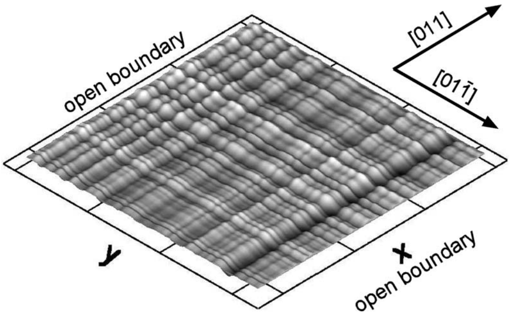

FIG. 8. Example of 16 μm × 16 μm simulated two-dimensional device. See for comparison the AFM topograph in Fig. 2.

$$S(x,y) = f_{[011]}(x) + f_{[01\bar{1}]}(y). \tag{9}$$

An example of a resulting surface is shown in Fig. 8.

As indicated in Sec. IV, the fluctuation distribution of the indium concentration follows the morphology of the surface, thus, the potential $V(x,y)$ that describes the fluctuations of the conduction band can be calculated as:

$$V(x,y) = k_v \times S(x,y), \tag{10}$$

where k_v is a proportionality constant (having physical dimension [eV/m]) that links the morphological fluctuations to the fluctuations of the conduction band.

The core of the numerical implementation is represented by the calculation of the scattering states of the potential $V(x,y)$ from which the transmission coefficient is obtained. This calculation is performed by means of the quantum transmitting boundary method.[36] In order to account for the size difference between the simulated and the experimental devices, we have investigated how the conductance scales with the size. Our simulations show that the conductance increases linearly with the width. In order to analyze the dependence upon the length of the sample, the contribution to $1/G$ due to the contacts[33]

$$\frac{1}{G_{\text{contact}}} = \frac{h}{2Me^2}, \tag{11}$$

where M is the number of the transverse modes entering in the contact, must be considered. After the subtraction of this contribution, $1/G$ decreases almost linearly with the length. Thus, the well-known equation $G = \gamma S/L$ (γ is the conductivity, S the cross section of the device, and L its length) is a good approximation and can be applied for our purposes.

VII. COMPARISON BETWEEN THEORY AND EXPERIMENTS

In the theoretical simulations, we have considered 40 different potential profiles randomly obtained with the procedure described above. The potential profiles are 80 μm wide squares. From each of these 40 profiles, we have selected one square region 4.5 μm wide. We have calculated the conductance along both crystallographic directions on each of these 4.5 μm wide devices. Then, we have calculated the average conductance values over the 40 devices. In Fig. 9, we plot the average values for $G_{[01\bar{1}]}$ and $G_{[011]}$ as a function of carrier density.

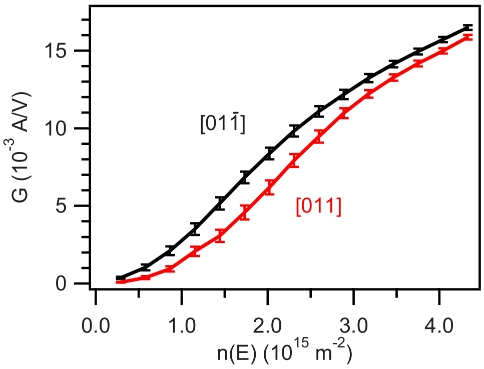

FIG. 9. (Color online) Average over 40 device conductances along the two crystallographic directions $[01\bar{1}]$ (black) and [011] (red). The error bars represent the error on the average. Each conductance value has been evaluated by means of Eqs. (5) and (10) with $m^\star = 0.03454 \times m_0$ and $k_v = 3.5 \times 10^6$ eV/m. In order to compare these results with the experimental ones, the conductances are plotted as a function of the 2D carrier density $n(E) = m^\star E/(\pi\hbar^2)$.

The absolute values of the average conductances obtained for both crystallographic directions are two/three times larger than the experimental ones (not shown in the graph), since in the simulations, we do not take into account all the possible scattering mechanisms that are instead present in the experiments. However, the remarkable difference between the two directions reproduces the anisotropy of the experimental results beyond the statistical error. In both directions, at low energy values, the conductance vanishes since the carriers entering into the device cannot tunnel through the thick (from 300 to 1100 nm) maxima of the undulated profile. On the other hand, when the carrier energy overcomes the energy of the highest peak, the barriers are less effective, the transmission coefficient $\tilde{T}(E)$ approaches 1, and, thus, the difference between the two curves is reduced.

The comparison between the simulated results and the experimental values of the conductances is performed by means of Eq. (3). In Fig. 10, we plot the quantity $\Delta(1/G)$ for the cases where $k_v = 2.75 \times 10^6$ and $k_v = 3.5 \times 10^6$ eV/m, together with the experimental curve. The two values for k_v correspond to a maximum peak to peak variation of the conduction band, ΔE_c, of 44 and 56 meV, respectively, on a simulated square profile 80 μm wide. As can be seen, the best agreement between experiment and simulation is obtained for a ΔE_c value of 56 meV.

VIII. DISCUSSION

The results of measurements and simulations are summarized in Fig. 11: the range of variation in indium concentration measured by PEEM (72.8%–77.9%) is indicated in the figure by the two vertical lines. The peak to peak variation of the conduction band, which best fits the asymmetry observed in the transport measurements (56 meV = ± 28 meV) is indicated in the figure by the horizontal lines. The black circles

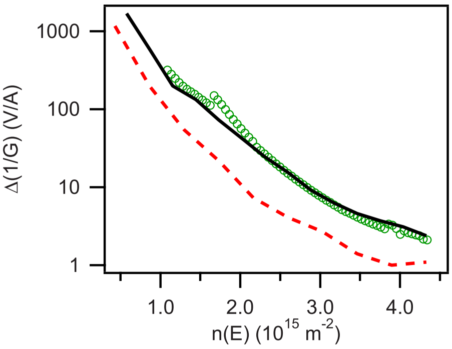

FIG. 10. (Color online) Plot of the $\Delta(1/G)$ curves. The dashed and continuous lines are obtained from simulations with $k_v=2.75\times10^6$ and $k_v=3.5\times10^6$ eV/m, respectively. Each curve has been obtained from the average conductance of 40 different simulated devices. The circles represent the experimental data of Fig. 4.

represent the energy variation of the CBM, $\Delta E_c(x)$ (44 meV$=\pm22$ meV at the PEEM range limits, as discussed in Sec. IV), as a function of the indium concentration. The good agreement between experimental PEEM results and the simulations leads us to conclude that a large fraction of the conduction band modulations can be attributed to indium concentration modulations.

Up to now, strain in the quantum well has not been considered. XRD data show that the quantum well region in this structure is, in average, nearly unstrained.[21] However, the lateral resolution of XRD is given by the x ray spot size ($\sim$1 mm^2), averaging the strain over a large area of the sample; thus, it cannot detect strain fluctuations at the micron scale. Compositional fluctuations around the XRD-determined average value may introduce strain modulations in the quantum well. In fact, strain modulations correlated with the surface cross-hatch pattern of lattice mismatched samples have been reported both for SiGe/Si[37] and for $In_xGa_{1-x}As$/GaAs with low In content.[38,39] If we assume that an $In_xGa_{1-x}As$ layer with local compositional fluctuation were grown on a perfectly uniform, strain-relaxed $In_{0.75}Al_{0.25}As$ substrate, a compressive strain would result in the In-rich areas, while a tensile strain would result in the In-poor areas. A compressive (tensile) strain increases (decreases) the band gap and increases (decreases) the CBM energy,[24] thus, reducing the effect of the bare compositional variation. Summing up the effects on the CBM of the indium concentration and of the strain modulation results in a $\Delta E_c(x)$ plot shown as crosses in Fig. 11. Clearly, the agreement between experiment and simulation is much worse, and so we can rule out the presence of a significant strain modulation.

IX. CONCLUSIONS

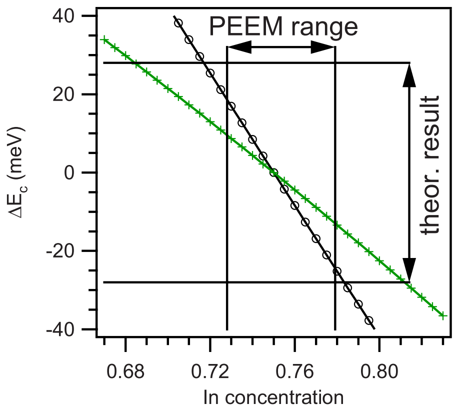

FIG. 11. (Color online) Conduction band energy variations due to indium concentration variations alone (circles) and due to the combined effect of concentration variations and consequent strain buildup (crosses). In the figure are indicated both the concentration variation range derived from the PEEM measurements and the ΔE_c value that best fits the transport data according to our simulations.

We have investigated a high mobility 2DEG formed in an $In_{0.75}Ga_{0.25}As$ QW, grown on lattice mismatched GaAs substrates. We have observed a strong transport asymmetry: the measured low-temperature electron mobility shows a pronounced difference between the $[01\bar{1}]$ and $[011]$ crystallographic directions. Laterally resolved photoemission measurements show a spatial modulation in indium concentration for the $In_{0.75}Ga_{0.25}As$ alloy, with a strong asymmetry in the two crystallographic directions. Through comparison with AFM topographs, we have shown that this modulation is correlated with the sample surface roughness. We have performed conductance calculations to verify if the transport asymmetry can be associated to the conduction band energy modulation correlated with the indium concentration. Good agreement is reached between the simulated and the measured transport asymmetry. We have, thus, identified the main origin of the transport asymmetry.

We have also demonstrated that this knowledge allows us to enhance the device performance by modifying the design of the grown structures: in fact, the reduction of the indium concentration modulation, through the insertion of a thin InAs layer in the QW, strongly suppresses the transport anisotropy and increases the overall electron mobility of the sample.

ACKNOWLEDGMENTS

The authors would like to acknowledge F. Capotondi, A. Bertoni, and G. Ferrari for fruitful discussions, and C. Murari and J.-Y. L'Excellent for the technical support to software development. Part of this work has been financed by the EU project "HYSWITCH," Contract No. 517567 of 6th Framework Programme.

*Present address: NEST CNR-INFM and Scuola Normale Superiore, 56126 Pisa, Italy. daniele.ercolani@sns.it

†Also at TASC CNR-INFM, 34012 Trieste, Italy

[1] M. J. Gilbert and J. P. Bird, Appl. Phys. Lett. **77**, 1050 (2000).
[2] D. Grundler, Phys. Rev. Lett. **84**, 6074 (2000).
[3] H. Hardtdegen, R. Meyer, H. Loken-Larsen, J. Appenzeller, T. Schäpers, and H. Lüth, J. Cryst. Growth **116**, 521 (1992).
[4] S. Gozu, C. Hong, and S. Yamada, Jpn. J. Appl. Phys., Part 2 **37**, L1501 (1998).
[5] P. Ramvall, N. Carlsson, P. Omling, L. Samuelson, W. Seifert, M. Stolze, and Q. Wang, Appl. Phys. Lett. **68**, 1111 (1996).
[6] T. Ando, A. B. Fowler, and F. Stern, Rev. Mod. Phys. **54**, 437 (1982).
[7] G. Bastard, Appl. Phys. Lett. **43**, 591 (1983).
[8] S. B. Ogale and A. Madhukar, J. Appl. Phys. **56**, 368 (1984).
[9] A. Gold, Phys. Rev. B **38**, 10798 (1988).
[10] K. Bhattacharyya, J. O. Orwa, and S. M. Goodnick, J. Appl. Phys. **73**, 4396 (1993).
[11] S. Tsujino *et al.*, Appl. Phys. Lett. **84**, 2829 (2004).
[12] P. Ramvall, N. Carlsson, P. Omling, L. Samuelson, W. Seifert, M. Stolze, and Q. Wang, Appl. Phys. Lett. **68**, 1111 (1996).
[13] P. Ramvall, N. Carlsson, P. Omling, L. Samuelson, W. Seifert, Q. Wang, K. Ishibashi, and Y. Aoyagi, J. Appl. Phys. **84**, 2112 (1998).
[14] F. Capotondi, G. Biasiol, D. Ercolani, and L. Sorba, J. Cryst. Growth **278**, 538 (2005).
[15] J. C. P. Chang, J. Chen, J. M. Fernandez, H. H. Wieder, and K. L. Kavanagh, Appl. Phys. Lett. **60**, 1129 (1992).
[16] R. S. Goldman, H. H. Wieder, K. L. Kavanagh, K. Rammohan, and D. H. Rich, Appl. Phys. Lett. **65**, 1424 (1994).
[17] A. Richter, M. Koch, T. Matsuyama, C. Heyn, and U. Merkt, Appl. Phys. Lett. **77**, 3227 (2000).
[18] S. Gozu, T. Kita, Y. Sato, S. Yamada, and M. Tomizawa, J. Cryst. Growth **227-228**, 155 (2001).
[19] S. Lohr, S. Mendach, T. Vonau, C. Heyn, and W. Hansen, Phys. Rev. B **67**, 045309 (2003).
[20] M. Rosini, E. Cancellieri, D. Ercolani, G. Biasiol, C. Jacoboni, and L. Sorba, Physica E (Amsterdam) **40**, 1392 (2008).
[21] F. Capotondi, G. Biasiol, D. Ercolani, V. Grillo, E. Carlino, F. Romanato, and L. Sorba, Thin Solid Films **484**, 400 (2005).
[22] F. Capotondi, G. Biasiol, I. Vobornik, L. Sorba, F. Giazotto, A. Cavallini, and B. Fraboni, J. Vac. Sci. Technol. B **22**, 702 (2004).
[23] I.-H. Tan, G. Snider, and E. Hur, J. Appl. Phys. **68**, 4071 (1990); see, also G. L. Snider's website at http://www.nd.edu/~gsnider/
[24] I. Vurgaftman, J. Meyer, and L. Ram-Mohan, J. Appl. Phys. **89**, 5815 (2001).
[25] K. H. Chang, R. Gilbala, D. J. Srolovitz, P. K. Bhattacharya, and J. F. Mansfield, J. Appl. Phys. **67**, 4093 (1990), and references therein.
[26] J. J. Yeh and I. Lindau, At. Data Nucl. Data Tables **32**, 1 (1985).
[27] G. Biasiol, S. Heun, G. B. Golinelli, A. Locatelli, T. O. Mentes, F. Z. Guo, C. Hofer, C. Teichert, and L. Sorba, Appl. Phys. Lett. **87**, 223106 (2005).
[28] S. Heun, G. Biasiol, V. Grillo, E. Carlino, L. Sorba, G. B. Golinelli, A. Locatelli, T. O. Mentes, and F. Z. Guo, J. Nanosci. Nanotechnol. **7**, 1721 (2007).
[29] N. W. Ashcroft and N. D. Mermin, *Solid State Physics* (Holt-Saunders, New York, 1976).
[30] I. Karpov, N. Venkateswaran, G. Bratina, W. Gladfelter, A. Franciosi, and L. Sorba, J. Vac. Sci. Technol. B **13**, 2041 (1995).
[31] O. Dehaese, X. Wallart, and F. Mollot, Appl. Phys. Lett. **66**, 52 (1995).
[32] J. M. Moison, C. Guille, F. Houzay, F. Barthe, and M. Van Rompay, Phys. Rev. B **40**, 6149 (1989).
[33] S. Datta, *Electronic Transport in Mesoscopic Systems* (Cambridge University Press, Cambridge, 1995).
[34] R. Landauer, Phys. Scr. **T42**, 110 (1992).
[35] R. Landauer, IBM J. Res. Dev. **32**, 306 (1988).
[36] C. Lent and D. Kirkner, J. Appl. Phys. **67**, 6353 (1990).
[37] D. E. Jones, J. P. Pelz, Y. Hong, I. S. T. Tsong, Y.-H. Xie, and P. J. Silverman, Appl. Phys. Lett. **69**, 3245 (1996).
[38] K. Rammohan, D. H. Rich, R. S. Goldman, J. Chen, H. H. Wieder, and K. L. Kavanagh, Appl. Phys. Lett. **66**, 869 (1995).
[39] N. Yamamoto, T. Mita, S. Heun, A. Franciosi, and J.-M. Bonard, *Optical Microstructural Characterization of Semiconductors*, MRS Symposia Proceedings No. 588 (Materials Research Society, Pittsburgh, 2000), p. 245.